Werk

Jahr: 1981
Kollektion: fid.geo
Signatur: 8 Z NAT 2148:50
Digitalisiert: Niedersächsische Staats- und Universitätsbibliothek Göttingen
Werk Id: PPN1015067948_0050
PURL: http://resolver.sub.uni-goettingen.de/purl?PPN1015067948_0050

LOG Id: LOG_0049
LOG Titel: Thermospheric winds during the energy budget campaign: ground-based fabry-perot observations supported by dynamical simulations with a three-dimensional, time-dependent thermospheric model
LOG Typ: article

Übergeordnetes Werk

Werk Id: PPN1015067948
PURL: http://resolver.sub.uni-goettingen.de/purl?PPN1015067948
OPAC: http://opac.sub.uni-goettingen.de/DB=1/PPN?PPN=1015067948

Contact

Niedersächsische Staats- und Universitätsbibliothek Göttingen
Georg-August-Universität Göttingen
Platz der Göttinger Sieben 1
37073 Göttingen
Germany
Email: gdz@sub.uni-goettingen.de

J Geophys (1982) 50:202–211

Journal of Geophysics

Thermospheric Winds During the Energy Budget Campaign: Ground-Based Fabry-Perot Observations Supported by Dynamical Simulations with a Three-Dimensional, Time-Dependent Thermospheric Model

D. Rees, P.A. Rounce, P. Charleton, T.J. Fuller-Rowell, I. McWhirter, and K. Smith
Department of Physics and Astronomy, University College London, Gower Street, London WC1E 6BT, United Kingdom

Abstract. Two very stable and sensitive Fabry-Perot interferometers were operated continuously throughout the period of the Energy Budget Campaign, at ESRANGE, Kiruna, to monitor the time-dependent variations of upper thermospheric (200–300 km) and lower thermospheric (90–120 km) winds, using the 630.0 nm and 557.7 nm forbidden lines of OI, respectively. Both instruments used vacuum-sealed etalons of 13 cm diameter with cemented spacers of 'Zerodur', providing a velocity reference stable to 10 m s^{-1}. Imaging photon detectors (based on a proximity-focused microchannel plate intensifier and resistive anodes) eliminated the use of pressure or piezoelectric scanning of the etalons and provided a sensitivity increase of a factor of ten over previous ground-based instruments. The high time-resolution data obtained during moderate auroral conditions ($\gtrsim$ 500 R, allowing 5 min per vector measurement) allows the rapid response of the thermosphere to geomagnetic substorms to be followed in detail. The continuous data obtained from both instruments is being used in conjunction with the University College London global, three-dimensional, time-dependent model of the thermosphere from the region of the mesopause upwards to understand the time-dependent energy and momentum sources of the thermosphere. A comparison of model and empirical data shows excellent agreement when low energy particle sources, concentrated in the auroral oval, are introduced to augment solar UV and EUV heating and polar energy and momentum sources associated with the magnetospheric electric field. During substorms the model predicts the generation of long-duration vortices in the lower thermosphere, but this cannot yet be confirmed by available experimental data. These vortices may have been observed during the latter part of the Energy Budget Campaign when simultaneous observations from Kiruna and Spitzbergen were possible. A joint analysis of these data sets and of the green line 557.7 nm data will be presented in a future paper.

Key words: Thermospheric winds – Auroral heating of upper atmosphere – Fabry-Perot interferometers

Introduction

Ground-based Fabry-Perot interferometers have been used for many years to observe the forbidden oxygen emissions of the upper atmosphere due to either airglow or auroral excitation mechanisms (Armstrong 1956; Chamberlain 1961). Of the many physical and chemical aeronomic quantities which may be studied on the basis of such observations, the thermal and dynamical structure of the upper mesosphere (OI 557.7 nm) and thermosphere (OI 630.0 nm) are of particular interest, and have been investigated by continuously-improving instrumental and data reduction techniques, particularly during the past twenty years (Armstrong 1969; Hays and Roble 1971a, b; Hernandez and Roble 1976a, b; Biondi and Fiebelman 1968; Nagy et al. 1974; Hays et al. 1969; 1979).

Very recently it has been possible to couple together major advances in Fabry-Perot etalon fabrication techniques, the development of imaging photon detectors (IPD) and the availability of low-cost, but powerful microcomputers, to build 'observatory-class' instruments which have the stability and sensitivity to measure temperature and vector winds with a time resolution of less than five minutes under mid-latitude airglow conditions. Under moderate auroral conditions (1 kR), a time resolution of less than 1 min can be obtained for a wind vector error of 10 m s^{-1}

To support the Energy Budget Campaign, two such Fabry-Perot interferometers (FPI) were run continuously from 28 October to 9/10 December 1980, at ESRANGE, Kiruna, Sweden. One of these instruments was used to observe the OI 630.0 nm line, monitoring F-region winds between about 200 and 300 km, while the second observed the OI 557.7 nm line to monitor winds in the lower thermosphere from about 100 to 120 km. Both instruments provided continuous data throughout the night of the *C* salvo of the Energy Budget Campaign on 10/11 November, and in the one hour period of most intensive auroral and rocket launching activity of the *A2* salvo of 1 December 1980. In addition, the data of many other nights of varied geomagnetic activity will be used to provide background information for thermospheric dynamics.

The University College London (UCL) three-dimensional, time-dependent model will be used to complement the ground-based and rocket-borne wind data, with their respective limitations to one height and to a short time period.

Adjustment of the 'open' parameters of the model, particularly the magnitude and extent of the polar electric field, auroral electron density and polar and auroral particle precipitation, will be necessary to fit the observed response to particular geomagnetic events. The data which is available from the two ground-based FPIs provides extended time coverage of the winds at 240 km and 100–120 km altitude, complementing the detailed height profiles from the rocket trails and falling spheres. Hence a representation of the complete time-dependent and three-dimensional time structure of the wind values for the N. Scandinavian and European regions can be obtained for each of the

0340-062X/82/0050/0202/$02.00

salvos (*C, B, A1* and *A2*), with one obvious limitation: for the *B* and *A1* salvos, since there were no wind measurements from the ground-based FPIs (owing to cloud cover at ESRANGE), the validity of the model results will be less than for the *C* and *A2* salvos where good ground-based data was available. However, since good ground-based data was obtained on other nights of activity comparable to those of the *B* and *A1* salvos, it is expected that a general predication of thermospheric dynamics can be obtained even for the *A1* and *B* salvos.

Instrumentation

The major advantages of the IPD in a Fabry-Perot interferometer (compared with a pinhole/photomultiplier detector) are:

1. The sensitivity improvement gained by integrating the entire Fabry-Perot image at all times. This improvement is, in practice, rather larger than the ratio of the number of steps per interferogram (20 to 32) divided by the ratio of the quantum efficiencies of a gallium arsenide photomultiplier photocathode to the S25 photocathodes we have been able to use within our present IPDs. Experience with operational photomultiplier and IPD systems would put the IPD advantage at a factor of about 10.
2. An extremely stable, non-scannable etalon can be fabricated and sealed in an evacuated chamber which is itself thermally controlled to about $\pm 0.2°$ C. The use of such a stable cavity considerably simplifies the data reduction procedure since frequent wavelength calibrations are not required. This simplifies the operating procedure of the interferometer, enhancing the already significant sensitivity gain due to the IPD itself.

Figure 1 shows, in schematic form, the optical and mechanical configuration of each of the two interferometers used during the Energy Budget Campaign. The specifications are summarized in Table 1. A computer-controlled scanning mirror system feeds light from a selected region of the sky directly into the 13 cm aperture etalon which is in a sealed and evacuated chamber. The entire first interference ring formed by this etalon is imaged via a Cassegrain telescope onto the photocathode of an IPD (Rees et al. 1980c; 1981) after passing through a 1 nm bandpass filter centered on 630.0 or 557.7 nm.

Table 1. Specification of 'red line' and 'green line' interferometers

Aperture	13.0 cm (coated full aperture except small area near 3×15 mm diameter spacers)
Etalon spacing	10 mm (Zerodur – cemented)
Reflection/Reflective finesse	86% (630 nm) ~20
Free spectral range	20 pm (at 600 nm)
Prefilter	1 nm (at 630.0 nm) 1 nm (at 557.7 nm) 60% peak transmission
Detector	Image Photon Detector 18 mm photocathode S20/S25 photocathode
Detected quantum efficiency at 630.0 nm at 557.7 nm	 4% 8%
Max. useful random event rate without pile-up	10 kHz, limited by electronics and A.D. converter
Spectral bins per free spectral range	~50
Effective finesse of complete system	8
Velocity stability of complete instrument: Long term drift Thermal drift	 < 1 m s^{-1} day^{-1} <40 m s^{-1} (°C)$^{-1}$
Residual pressure in etalon cavity	40 torr (for tuning Fabry-Perot ring pattern of the IPD)
Thermionic emission rate at operational temperature of 10° C	~60 s^{-1} from entire photocathode

All of these optical elements are individually mounted onto four 22 mm diameter steel rods, which are themselves mounted onto an optical bench (Fig. 2). In use, the optical bench is mounted vertically, and the scanning mirror system is mounted

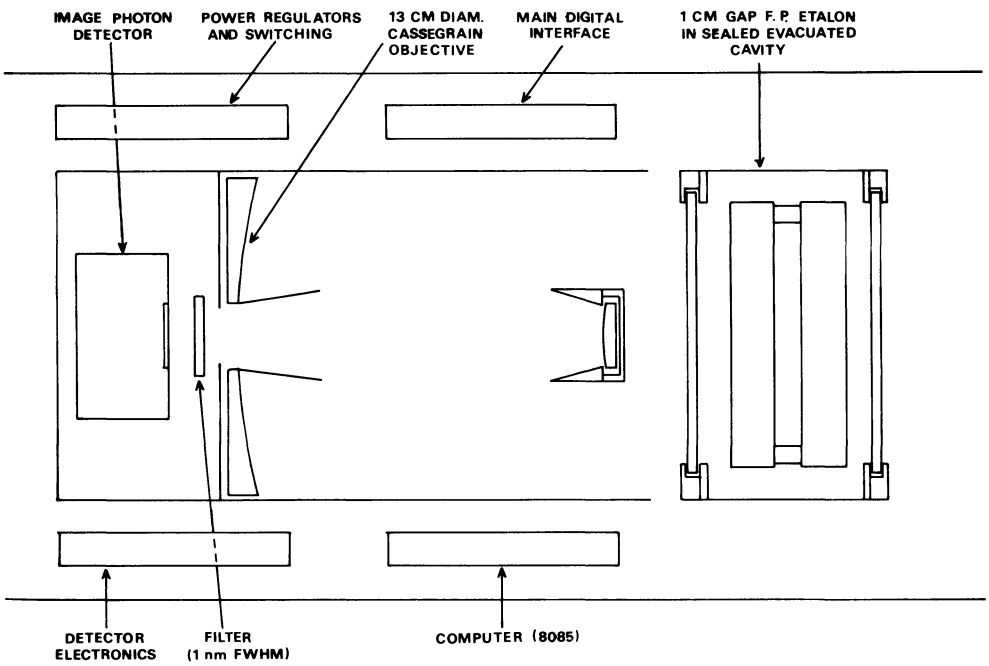

Fig. 1. Schematic configuration of the UCL ground-based Fabry-Perot interferometers used in the Energy Budget Campaign

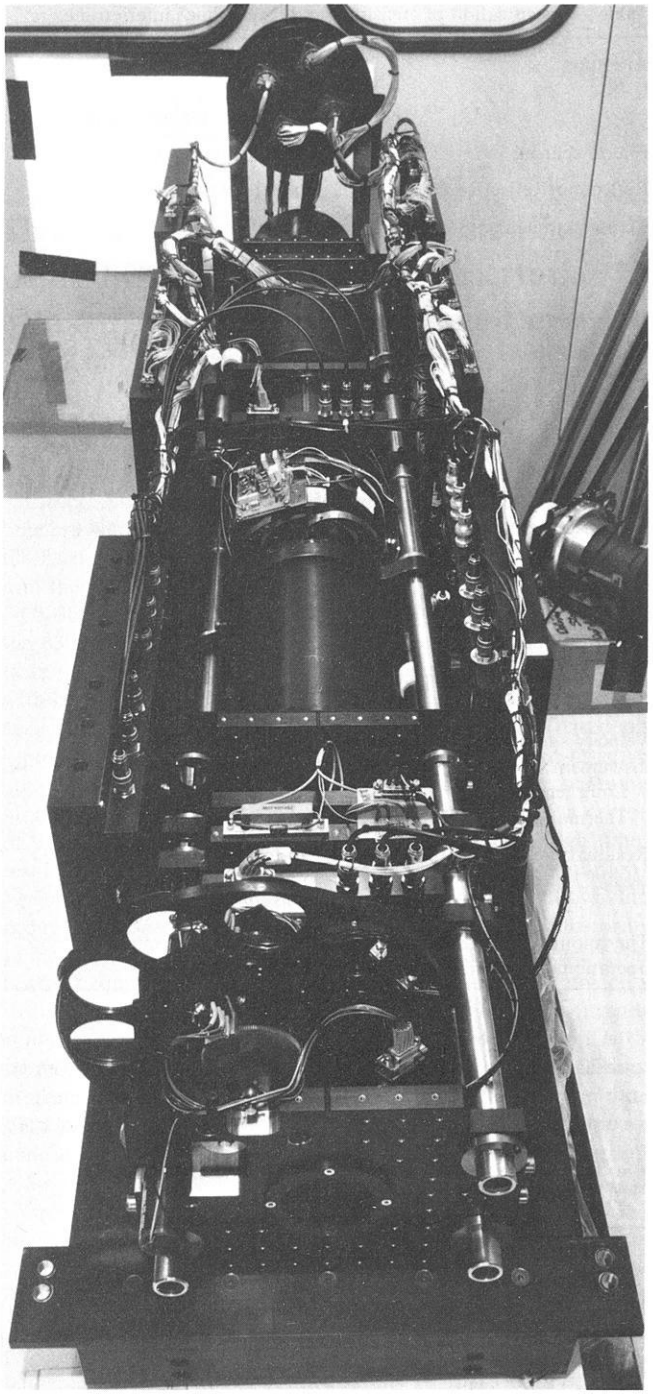

Fig. 2. Photograph of the UCL balloon-borne Fabry-Perot interferometer showing method of construction of the double optical bench arrangement

on top of the optical bench. A light shield is mounted immediately around the main optical components, and several baffle plates are used, both internally and externally, to preclude scattered light reaching the IPD.

The main instrument electronics (Fig. 1) is mounted on the optical bench in five boxes immediately around the sides of the optical assembly, and the entire assembly is completely covered by another light shield. All mechanical components are matt black anodised except for the four steel rodes which are chrome-plated to ensure ease of assembly and adjustment. The entire optical assembly is very rigid and is not noticeably affected by thermal changes within the range of about 15° C ± 5° C, except for etalon changes which are avoided by thermal control of the entire sealed etalon mount to ±0.2° C.

The optical assembly is extremely stable in use – no detectable changes in the image were discerned over 6 weeks observing during the Energy Budget Campaign. One of the systems was demounted as a complete unit at the end of this campaign and transported by car to United Kingdom and has since been operated continuously as a mid-latitude observatory instrument without requiring any readjustment of etalons, optics or electronics.

The etalon construction is based on techniques developed for the NASA Dynamics Explorer Fabry-Perot interferometer (FPI) – a collaboration between the University of Michigan (Professor P.B. Hays) and University College London.The etalon plates are cemented together using three identical spacers made of Zerodur (a ceramic material of extremely low thermal expansion coefficient, made by Schott). The cementing process, which is carried out after the etalon has been tested as an optically-contacted device, used a UV setting cyano-acrylic 'super-glue' or a similar material such as 'Norland 61', which leaves considerable flexibility to the operator in obtaining a parallelism of better than $\lambda/40$ in the finally assembled etalon. Exhaustive tests have shown that an effective coefficient of expansion of less than 5×10^{-8} ($°C^{-1}$) can be achieved by batch selection of the Zerodur. Such an etalon is also extremely stable in both short and long term in respect of drifts and thermal behaviour. The cemented bonds will easily withstand stresses applied to the etalon which (at levels >300 N) permanently strain the etalon plates. In practice the complete etalon is mounted within a cantilevered unit which allows the fine tuning of the parallelism of the etalon without imparting thermal changes of the mount to the etalon. This mount is also designed to be sealed and evacuated without transmitting the strain of the evacuated outer section to the inner mounting which actually supports the etalon. Finally, this mount provides essential mechanical support to the etalon to withstand shocks and vibration encountered during transportation.

Signal Processing and Data Analysis System

Figure 3 illustrates the general electronic signal processing configuration used to provide on-line interactive colour graphics display of the raw data, and several levels of image processing and analysis. The raw IPD data is accumulated photon by photon in the 8K (kilobyte) RAM (random access memory) of the 8085 microcomputer of the FPI itself. Features such as integration time and view direction are commandable either interactively or automatically. A complete image is transmitted to the main microcomputer – OSI C3-OEM (56K RAM) – at the end of each frame, where a wide variety of image analysis procedures can be called up, again, either interactively or automatically. These include scaling the image for colour-graphic representation (Fig. 4), 'reduction to radius' – which is the corrected observed spectrum reduced to wavelength by integrating annular rings of uniform area outward from the geometric centre of the Fabry-Perot ring pattern – with display of the reduced spectrum and many other analytical aids summarized in Table 2.

The mass storage device is a dual 8″ diskette (single side, single density) which allows storage of about 70 complete images when running automatically. It is not usually necessary to store the entire image, however, due to the stability of the system, and a more economical procedure of only storing the reduced spectrum plus the associated analysis is normally used. In this mode the data and results of six complete nights of observation,

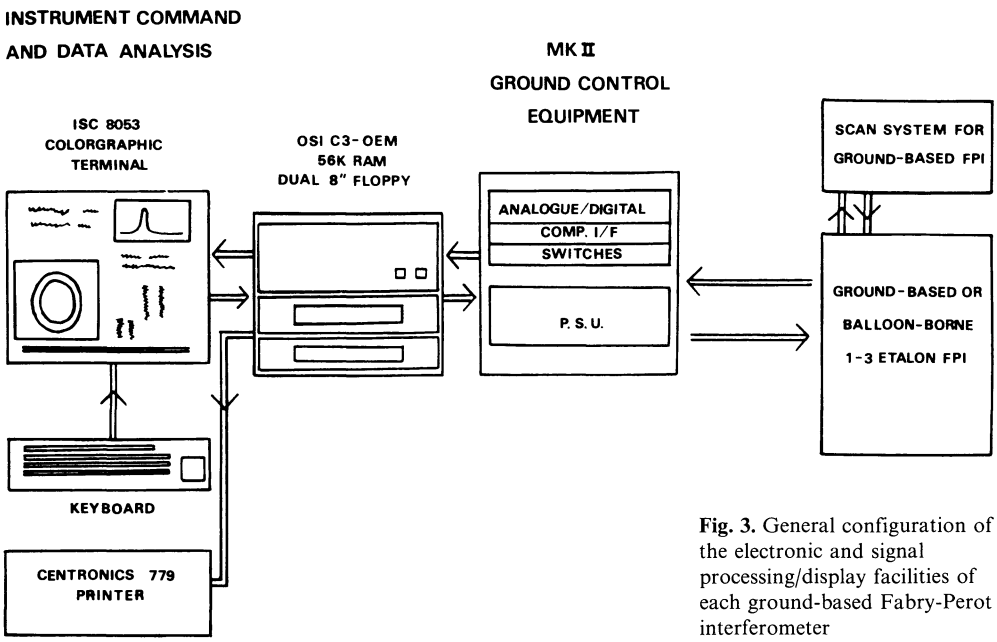

Fig. 3. General configuration of the electronic and signal processing/display facilities of each ground-based Fabry-Perot interferometer

Table 2. Summary of interactive and automatic image analysis and display function of the OSI and ISC facility

Function	Parameters	Operation
Image	Background (nn)/**scale** (mm)	Performs linear conversion of photon image to 8-colour graphics display with variable background subtraction (nn) and intensity level scaling (mm)
Clock	"HH MM SS" on "DD MM YY"	Sets 100 year, real time, clock
Mirror "Direction"	N, E, S, W	Manual direction control of mirror
Mirror rotate after 'M' "Direction"	N, E, S, W	Automatic direction control of mirror
Display	H, V, 'M'	Performs and displays slice horizontally or vertically through image; automatically scales residual in top right hand corner of video display
Subtract		Generalized function which can be used to correct fully for thermionic emission and non-uniform sensitivity of detector and display or to reduce functions
Store 1, 2		Calibration data used as basis for 'Subtract'
Reduce		For Fabry-Perot operations: reduces and displays the total X, Y, photon image data set as an integrated spectrum vs wavelength; corrects for geometrical properties of X, Y vs R, θ co-ordinates
LSQ		Least square quadratic fit over specified 'limits' for quick-look analysis of wavelength or velocity
Analyse		Equal areas fit to data for wavelength or velocity. Useful after generalized correction of photometer data by 'Subtract'
Time	Seconds	Controls length of integration period from 1 s up to 65000 s
Message	"Any comment"	Note pad
List	All, plot, radius	Used for printer listing of image, reduced data etc.
Disk	On/off drive, track	Specifies disk record (automatic log) of data in interactive or automatic modes
Printer	On/off	Printer command
Countsave	On/off	Stores full image, or reduced spectrum on disk at end of each frame

at two minutes integration time per image, can be stored within the two available diskettes (2×275 K).

A 110 character per second (parallel) printer is used to log all operations (this information is also stored on disk) such as real time clock, frame number, integration time, view direction and any information which has been stored manually (auroral/weather conditions etc.). Normally, the results obtained from the automatic analysis algorithms are also printed out, with the reduced spectrum, as well as being stored on disk. Subroutines are used for subtracting thermionic emission from the im-

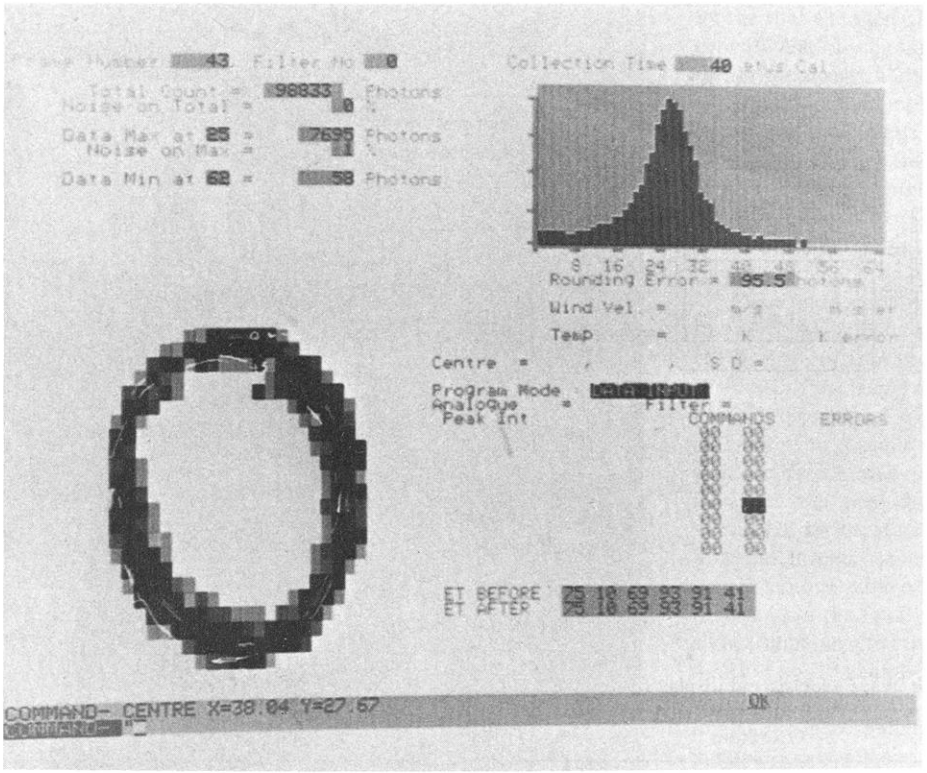

Fig. 4. Photograph of graphic terminal output

age, which may be an important factor when long integration periods are used at times of weak airglow/auroral emissions (i.e. 100 R or less).

The UCL Three-Dimensional, Time-Dependent Model

A three-dimensional, time-dependent thermospheric model has been developed at UCL to follow the complex reaction of the thermosphere to a wide range of both global and local energy and momentum sources (Rees et al. 1980a; 1980b; Fuller-Rowell and Rees 1980; 1981).

The model is entirely self-consistent in treating the neutral gas equations of motion except that, at present, only a single constituent is considered, whose mean molecular weight is a variable, dependent only on pressure. The energy sources considered are solar EUV, using most recent sources of solar flux and EUV heating efficiency of Hinteregger (1979) and Torr et al. (1980) respectively, and particulate heating associated with the polar cap region – of importance during geomagnetically quiet periods – and Joule and particulate heating associated with the auroral oval and which is strongly enhanced during geomagnetic substorms. Momentum sources are the polar cap and auroral oval magnetospheric electric field sources (Heppner 1977), which are related to geomagnetic activity, and a low- to mid-latitude 'dynamo' electric field (Richmond et al. 1980) related to seasonal and solar activity. A global electron density model due to Ching and Chiu (1973) and Chiu (1975) is adapted in an ad hoc manner to respond to geomagnetic auroral activity. The electron density/ionospheric model is not yet fully self-consistent, due to the difficulty of solving the extra equations and the lack of adequate global data with which to test predictions. Basically, the three-dimensional electron density structure is modified to produce realistic auroral electrojets consistent with the polar and auroral electric field structure.

Figure 5 shows a steady-state winter distribution of wind at 120 and 240 km altitude, while Fig. 6 shows the corresponding winds 80 min after the onset of a substorm which would create a 500 γ disturbance under the electrojet in the midnight region of the auroral oval.

The model also predicts the temperature and density distributions at all altitudes from 80 to about 500 km and, in the near future, we expect to be able to extend the calculations to cope with two constituents (O and N2). In the context of the Energy Budget Campaign, the model will be used to complement and extend the wind data obtained from ground-based and rocket techniques and to calculate transport and dissipation rates of energy, momentum and minor species.

Typical Observations

One or both Fabry-Perot instruments were in operation every night from 30/31 October to 8/9 December inclusive, providing some 350 diskettes of data (100 megabytes total). While the quick-look analysis of this data is carried out and logged in real time, providing a good estimate of the magnitude and direction of the wind vectors, the final analysis of this large amount of data will not be complete for several months.

Figures 7, 8 and 9 show the wind data obtained during parts of the nights of 10/11, 19/20 and 29/30 November, respectively. These nights had substantial auroral and geomagnetic activity so that the instruments were able to make measurements in each of four directions, N, E, S and W, within a period of 6 min. Due to the high time resolution, and the significance of each individual measurement, each of the four measurements is plotted individually as two separate measurements of both the zonal and the meridional winds, looking east and west, and north and south, respectively. Assuming that the mean emission altitude is 240 km, then, at zenith distance, the horizontal separation of these data points is of the order of 800 km, some 7°.5 of latitude, or $1^1/_2$ h of local time. Also shown in Figs. 7, 8

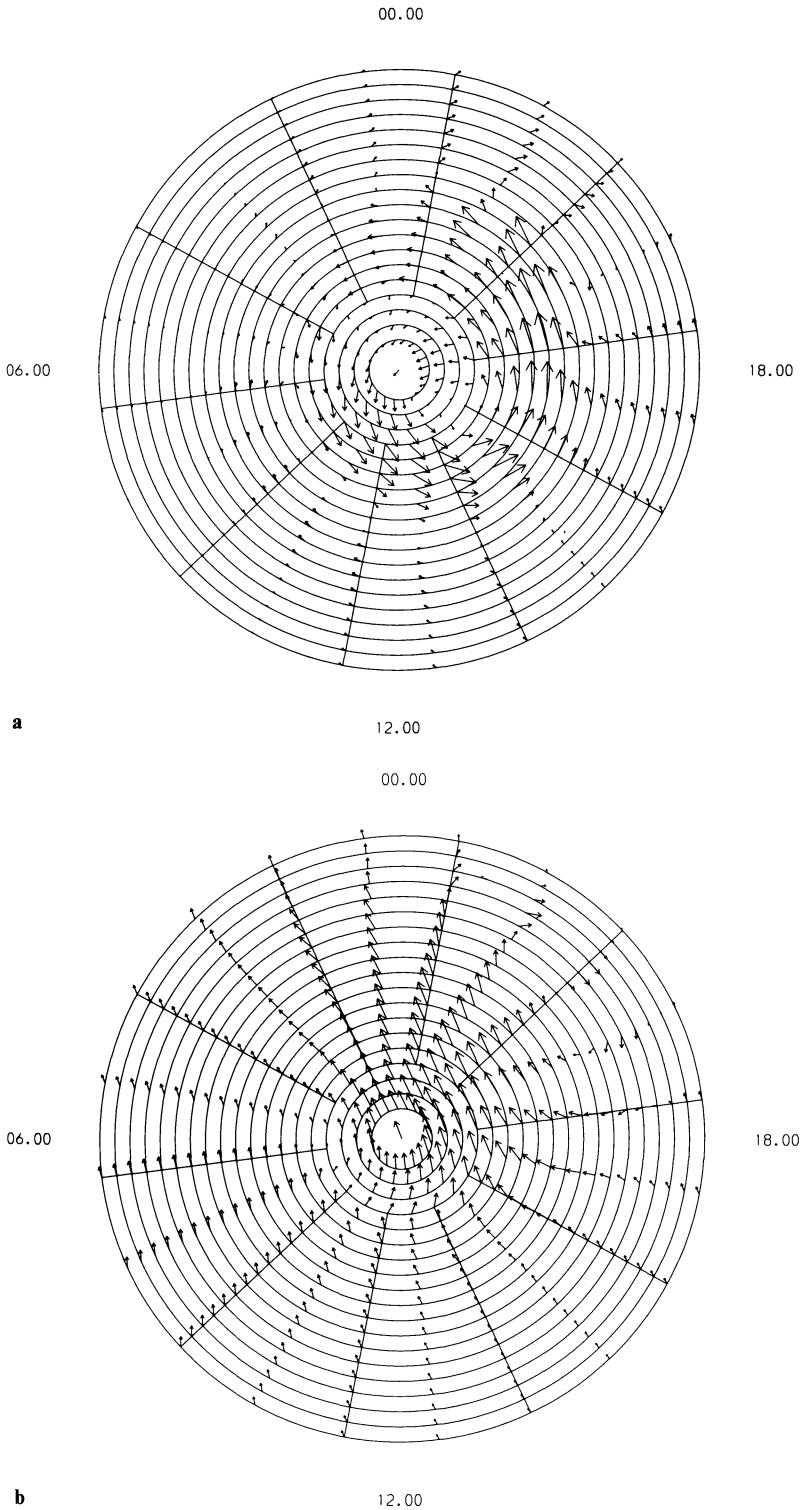

Fig. 5a and b. Wind velocities for the northern hemisphere poleward of 50° N, steady-state conditions at 0030 UT, roughly corresponding to the onset of the substorm of salvos *A*1 and *A*2. The Figs. show geographic co-ordinates at 2° latitude and 1.2 h local time spacings, and at altitudes **a** 120 km (40 m/s ≡ 2° lat.); and **b** 240 km (160 m/s ≡ 2° lat.)

and 9 are the steady-state meridional and zonal winds generated by the UCL model for winter conditions, and the relevant geomagnetic and solar activity conditions for the geographic and geomagnetic location of Kiruna.

Examination of Figs. 5 and 6 shows that large changes of the horizontal wind are expected over horizontal distances of this magnitude, and Figs. 7, 8 and 9 show that these large differences do exist. Figures 7, 8 and 9 also show that the horizontal gradients of the meridional winds (measured in the north and the south) and the zonal winds (measured in the east and the west) increased during disturbed periods as would be expected (Figs. 5 and 6). A comparison of the steady-state model and observed winds shows that ground tracks of the observed winds follow the predicted behaviour very well, with the exception of the short-timed perturbations which are associated with the effects of individual or sequential geomagnetic substorms.

One factor which we can estimate from the three-dimensional, time-dependent model is the possible contribution of large verti-

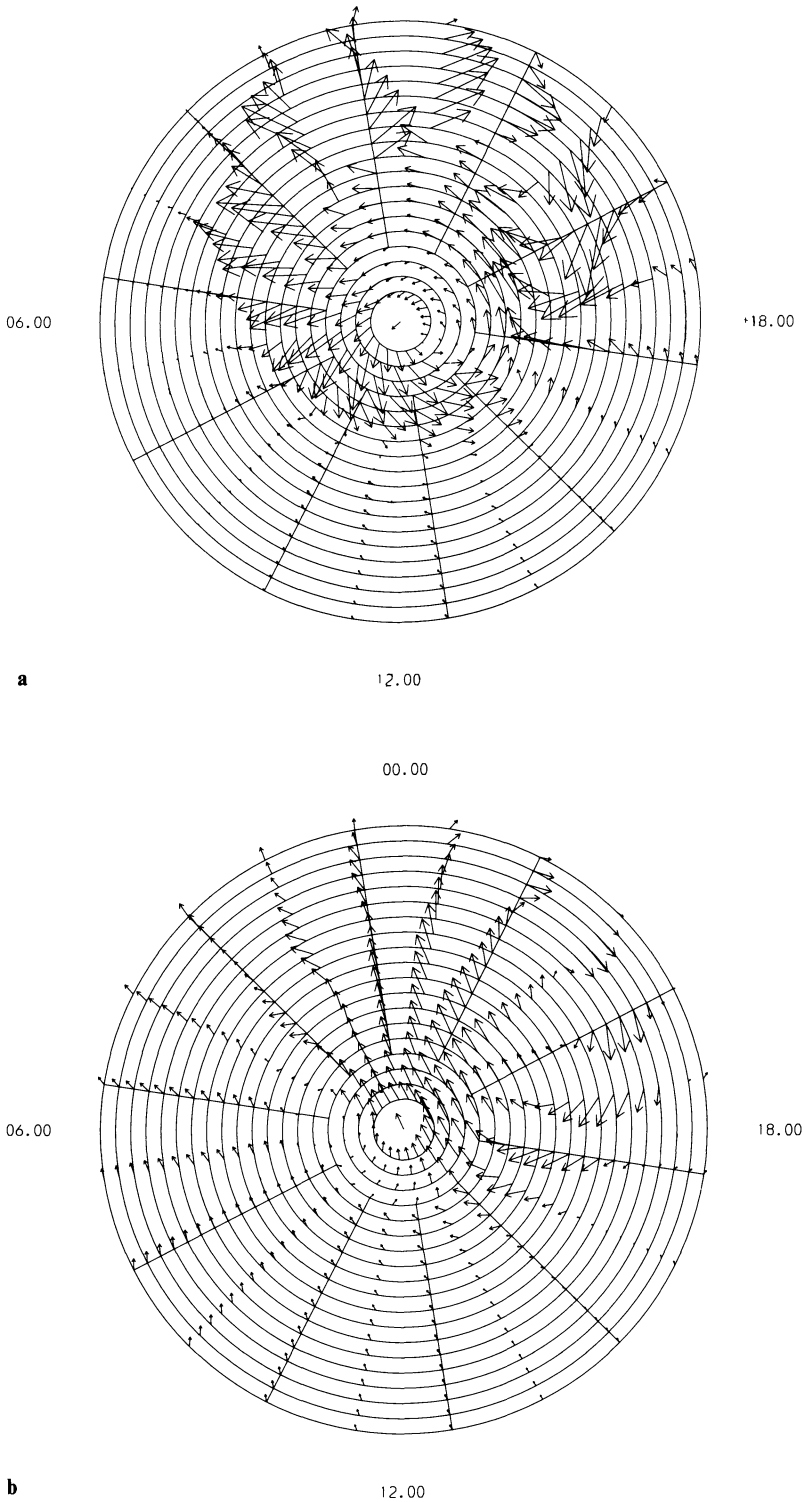

Fig. 6a and b. As for Fig. 5, but 80 min after the onset of the modelled substorm, approximating to the substorms of salvos *A*1 and *A*2, for altitudes **a** 120 km (40 m/s ≡ 2° lat.) and **b** 240 km (160 m/s ≡ 2° lat.)

cal convective F-region winds. At times such as 0200 UT on 30 November 1980, our three-dimensional, time-dependent model predicts that mean and large-scale upward winds near 300 km in excess of 10 m s^{-1} may have been present. Due to the likely large horizontal gradients of the vertical wind and its rapid temporal changes in response to geomagnetic activity, it is not practical to attempt to correct for the vertical wind by means of a single measurement at the local zenith.

The maximum contribution δ of vertical winds to the data of Figs. 7, 8 and 9 is likely to be less than

$Vz_{MAX} \cos \varphi$

where $Vz_{MAX} < 50$ m s^{-1}

and the viewing angle to the zenith, ϕ, is 60°, so that

$\delta \approx 25$ m s^{-1}

It is thus of negligible significance in terms of the zonal and meridional wind components at the onset of the 500 γ substorm near 0300 LT on 30 November (Fig. 9a and 9b).

Between 0230 and 0300 LT, as the substorm builds up, with

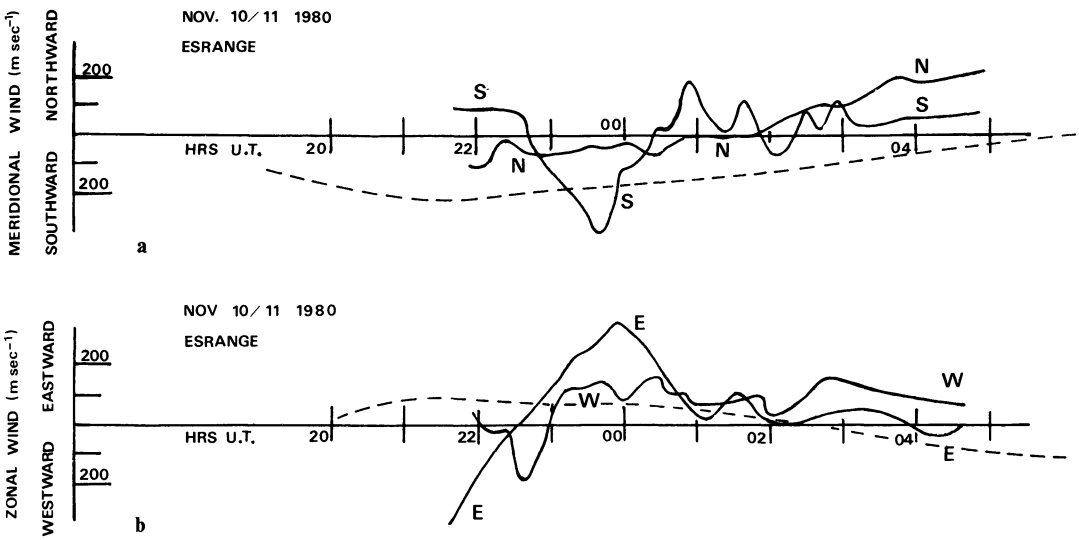

Fig. 7a and b. **a** Meridional and **b** zonal measurements about 400 km north (N), east (E), south (S) and west (W) respectively of Kiruna, as obtained directly by scanning the Fabry-Perot at 60° zenith distance. Time resolution between individual measurements in a single direction is 6 min. The dashed line shows the theoretical steady-state wind predicted by the UCL three-dimensional, time-dependent model. Data for 10/11 November 1980

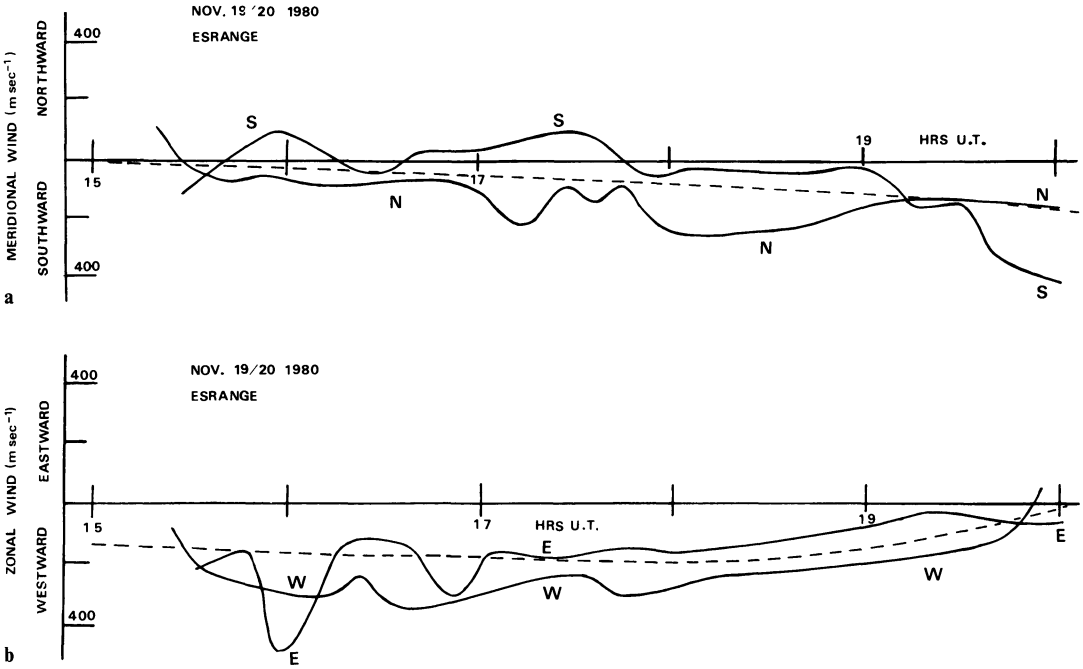

Fig. 8a and b. As Fig. 7, for 19/20 November 1980

most of the auroral activity (and therefore heating) to the south of Kiruna, the zonal wind to the east of Kiruna increased from 200 to 330 m s^{-1} At the same time, while the meridional winds to the south, and the zonal winds to the east changed only slightly, the meridional wind measured to the north decreased from being southward at 300 m s^{-1}, reversed sense, and reached a maximum poleward value of nearly 100 m s^{-1}. As the auroral and magnetic activity decayed after 0300 LT, the zonal wind to the east decreased again, while the meridional wind north of Kiruna again became southward reaching a maximum value of 300 m s^{-1} at 0330 UT.

This one hour period presented a fascinating picture of the dynamical response of the thermosphere to intense and localized auroral heating, where the high time-resolution of the new instruments unambiguously followed in detail the consequence of the substorm in a way which has not been possible with earlier instruments.

Apart from the rapid and significant changes of zonal and meridional winds which correlate well with discrete substorm activity, general trends are visible in both Fig. 8 and 9. In the early evening, when the meridional winds are usually less than 100 m s^{-1}, there is a strong westward wind driven by the ion drag of the westward convecting ions (northward electric field). By about 1900 to 2000 LT, an equatorward wind becomes obvi-

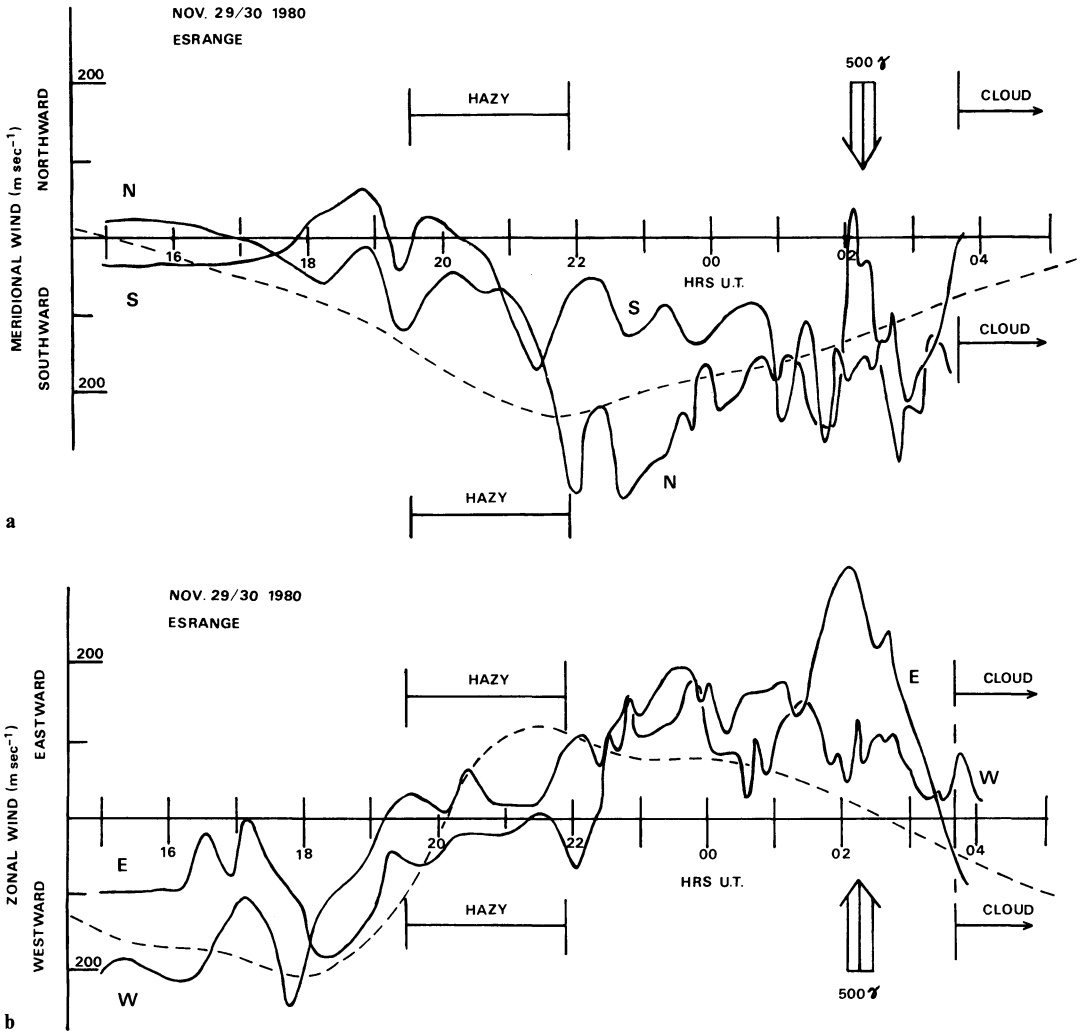

Fig. 9a and b. As Fig. 7, for 29/30 November 1980

ous, given even a modest level of geomagnetic activity, while the zonal wind reverses to become eastward between 2000 and 2100 LT.

Except for these general trends, which correlate in magnitude with the onset of geomagnetic activity, the detailed response of the winds measured respectively N and S, and E and W, of Kiruna, is not well correlated on time scales of up to ~1 h, reflecting the detailed temporal and spatial structure of the auroral momentum and energetic source.

Acknowledgements. The operation of the two Fabry-Perot interferometers at ESRANGE was greatly facilitated by the assistance and facilities made available, in particular, by Mr. Lars Larsson and Mr. Bengt Dahlstadt, and the co-ordinating activities of Professor D. Offermann and the DFVLR management.

We should also like to acknowledge a number of valuable technical and scientific discussions with Professor P.B. Hays and Dr. R.W. Smith in respect of the design and operation of Fabry-Perot interferometers at stations within the auroral oval.

This work was supported by Grants from the United Kingdom Science Research Council.

References

Armstrong, E.B.: In The Airglow and the Aurorae, E.B. Armstrong and A. Dalgarno, eds.: pp 366–373. New York: Pergamon, 1956

Armstrong, E.B.: Doppler shifts in the wavelength of the IO 6300 line in the night airglow. Planet. Space Sci. **17**, 957–974, 1969

Biondi, M.A., Fiebelman, W.A.: Twilight and nightglow spectral line shapes of the oxygen λ6300 and λ5577 radiation. Planet. Space Sci. **16**, 431–443, 1968

Chamberlain, J.W.: Physics of the Aurorae and Airglow. New York: Academic Press 1961

Ching, B.K., Chiu, Y.T.: A phenomenological model of global ionospheric electron density in the E, F_1 and F_2 regions. J. Atmos. Terr. Phys. **35**, 1615–1630, 1973

Chiu, Y.T.: An improved phenomenological model of ionospheric density. J. Atmos. Terr. Phys. **37**, 1563–1570, 1975

Fuller-Rowell, T.J., Rees, D.: A three-dimensional, time-dependent, global model of the thermosphere. J. Atmos. Sci. **37**, 2545–2567, 1980

Fuller-Rowell, T.J., Rees, D.: A three-dimensional, time-dependent simulation of the global response of the thermosphere to a geomagnetic substorm. J. Atmos. Terr. Phys. **43**, 701–721, 1981

Hays, P.B., Meriwether, J.W., Roble, R.G.: Night-time thermospheric winds at high latitudes. J. Geophys. Res. **84**, 1905–1913, 1979

Hays, P.B., Nagy, A.F., Roble, R.G.: Interferometric measurements of the 6300 Å Doppler temperature during a magnetic storm. J. Geophys. Res. **74**, 4162–4168, 1969

Hays, P.B., Roble, R.G.: A technique for recovering Doppler line profiles from Fabry-Perot interferometer fringes of very low intensity. Applied Optics **10**, 193–200, 1971 a

Hays, P.B., Roble, R.G.: Direct observations of thermospheric winds during geomagnetic storms. J. Geophys. Res. **76**, 5316–5321, 1971 b

Heppner, J.P.: Empirical models of high latitude electric fields. J. Geophys. Res. **82**, 1115–1125, 1977

Hernandez G., Roble, R.G.: Direct measurements of nighttime thermospheric winds and temperatures. 1. Seasonal variations during geomagnetic quiet periods. J. Geophys. Res. **81**, 2065–2074, 1976a

Hernandez G., Roble, R.G.: Direct measurements of nighttime thermospheric winds and temperatures. 2. Geomagnetic storms. J. Geophys. Res. **81**, 5173–5181, 1976b

Hinteregger, H.E.: Development of Solar Cycle 21 observed in EUV spectrum and atmospheric absorption. J. Geophys. Res. **84**, 1933–1938, 1979

Nagy, A.F., Cicerone, R.J., Hays, P.B., McWatters, K.D., Meriwether, J.W., Belon, A.E., Rino, C.L.: Simultaneous measurement of ion and neutral motions by radar and optical techniques. Radio Sci. **9**, 315–321, 1974

Rees, D., Fuller-Rowell, T.J., Rounce, P.A.: Asymmetric global circulation systems following geomagnetic substorms. Proc. Vth ESA-PAC Symposium on European Rocket and Balloon Programmes and Related Research, Bournemouth, 1980. ESA SP-152 June 1980, 81–88, 1980a

Rees, D., Fuller-Rowell, T.J., Smith, R.W.: Measurements of high latitude thermospheric winds by rocket and ground-based techniques and their interpretation using a three-dimensional, time-dependent dynamical model. Planet. Space Sci. **28**, 919–932, 1980b

Rees, D., McWhirter, I., Rounce, P.A., Barlow, F.E., Kellock, S.J.: Miniature Imaging Photon Detectors. J. Phys. E: Sci. Instrum. **13**, 763–770, 1980c

Rees, D., McWhirter, I., Rounce, P.A., Barlow, F.E.: Miniature Imaging Photon Detectors. II. Devices with transparent photocathodes. J. Phys. E: Sci. Instrum. **14**, 229–233, 1981

Richmond, A.D., Blanc, M., Emery, B.A., Wand, R.H., Fejer, B.G., Woodman, R.F., Ganguly, S., Amayenc, P., Behnke, R.A., Calderon, C., Evans, J.V.: An empirical model of quiet-day ionospheric electric fields at middle and low latitudes. J. Geophys. Res. **85**, 4658–4664, 1980

Torr, M.R., Torr, D.G., Richards, P.G.: The solar ultra-violet heating efficiency of the midlatitude thermosphere. Geophys. Res. Lett. **7**, 373–376, 1980

Received June 26, 1981; Revised version October 26, 1981
Accepted November 18, 1981